Optically Quantifying Spatiotemporal Responses of Water Injection-Induced Strain via Downhole Distributed Fiber Optics Sensing

Yankun Sun[1, 2], Ziqiu Xue[1, 2], Tsutomu Hashimoto[1, 2], Yi Zhang[1, 2]

[1]Geological Carbon Dioxide Storage Technology Research Association, 9-2 Kizugawadai, Kizugawa-shi, Kyoto 619-0292, Japan

[2]Research Institute of Innovative Technology for the Earth, 9-2 Kizugawadai, Kizugawa-shi, Kyoto 619-0292, Japan

Corresponding author: Yankun Sun, sun@rite.or.jp.

Key Points:

- Novel hybrid fiber optics is exploited to distributed monitor strain responses along a 300-m borehole in a fibered injection well.
- Clear-cut spatiotemporal strain profiles/fronts in one water injection section have been captured via one single sensor cable.
- Combined effects of injection scenario on injection-induced strain are first explored quantitatively.

Abstract

Harsh subsurface environment limits robust workability of on-site instrumentation to be leveraged to track solid Earth's dynamics. Distributed fiber-optic sensing technology (DFOS) allows long-period in-situ real-time detection of crustal geoenergy exploration-induced underground motions. Here, we first deployed 300-m-long fiber-optic cables

behind casing of an actual injection well via single-ended, hybrid Brillouin-Rayleigh backscatterings interrogator to distributed monitor water injection test between two adjacent wells in onshore Mobara, Japan. Detailed DFOS recordings over the entire borehole visualized clear-cut spatiotemporal strain responses from one water injection. Potential injected water-transport footprint and impacted zone reasonably coincided with those of analogy-based strain fronts. Our study thus further uncovered that injection volume and injection pressure significantly dominated water injection-driven strain magnitude and coverage.

Plain Language Summary

Distributed fiber optic sensing is an emerging technique to monitor dense geophysical information inside the Earth. This study explores in greater detail spatiotemporal strain evolutions from one water injection process in an actual 300-m-deep well via FO cables based on hybrid Brillouin-Rayleigh backscatterings at unprecedented resolution. Clear-cut strain profiles portray water migration footprints, and observed strain fronts are good agreement with impacted extent. Measurable strain magnitude and evolutions closely depend on injection scenario. These findings open up a new avenue for finely optical geoenergy monitoring and fluid evolution imaging that boost all-optical early-warning potential and quantitative risk decision-making for future quasi-geodetic strain-related geohazards.

1. Introduction

Massive fluids injection and/or production such as CO_2 geological storage (CGS) and groundwater withdrawal often pose pore pressure perturbation, ultimately resulting in near-surface geomechanical deformation (i.e., strain): ground uplift or subsidence. Moreover, fluid injection-induced deformation can potentially create or reactivate fractures and faults in reservoir-caprock systems, thereby triggering unfavorable leakage pathways or microseismic/felt-earthquake occurrence (Baatz et al., 2015; White et al., 2014; Zoback and Gorelick, 2012). Monitoring in-situ deformation/strain distributions from injection reservoirs to surface is thus important to obtain a complete understanding of crustal geomechanics in various near-surface geoengineerings.

Typical strain-recording instruments utilized in various CGS sites mainly include global positioning system (GPS) (Karegar et al., 2015; McColpin, 2009), interferometric synthetic aperture radar (InSAR) (Ferretti et al., 2011; Vasco et al., 2010), tiltmeter (Murdoch et al., 2019; Siriwardane et al., 2013), seismic/microseismic geophones (Arts et al., 2004; Chadwick et al., 2004; Saito et al., 2006; Verdon et al., 2015). However, these instrumentations possess low resolution, small coverage, high cost, discrete detection, time-consuming, short term, poor signal-to-noise ratio (SNR), etc. (Verdon et al., 2013), apart from subsurface complexity, limiting us to refine images of deep reservoir geomechanical responses (Jousset et al., 2018). Hence full- depth strain profiles regarding precisely how the near-wellbore strata deform vertically at higher spatial and temporal resolution in CO_2 storage environments are unclear. Despite efforts aimed at developing CGS-related downhole sensors, some challenges remain

poorly addressed, including high-pressure high-temperature (HPHT), stronger corrosivity, indirect and point detection, etc. (Arts and Vandeweijer, 2011; Baldwin, 2014b; Shanafield et al., 2018).

Distributed fiber-optic sensing (DFOS) technologies, an emerging technology that turns optical fiber into an array of sensors, allows for densely distributed strain measurement along a single fiber optic (FO) cable (Bao and Chen, 2012; Kogure and Okuda, 2018; Miah and Potter, 2017). One major benefit of DFOS is that it can record the measurands (e.g., temperature, strain, pressure, vibration and acoustics) as a function of the position along the entire FO length (Schenato, 2017). Distributed temperature sensing (DTS) with Raman scattering, Brillouin/Rayleigh scattering-based distributed strain sensing (DSS) and distributed acoustic sensing (DAS) with Rayleigh scattering are the most frequently-used DFOS in the oil and gas industry for many decades (Kersey, 2000). However, only a few studies have explored DFOS potential for downhole sensing applications (Bense et al., 2016; Karrenbach et al., 2017; Lellouch et al., 2019).

Recently, DFOS has been introduced to monitor CGS-related small strains in laboratory and field tests. Zhang et al., (2019) and Zhang and Xue (2019) observed CO_2 plume or brine migration behaviors in a Tako sandstone core via Rayleigh-based DFOS and X-ray computed tomography. Lei et al., (2019) and Xue et al., (2018) deployed three FO cables behind casing to sense strain responses from pumping water in two neighboring wells. Sun et al., (2019) measured in-situ strain distributions induced by water injection

tests performed in a well close to the fibered well. These lab-field investigations push DFOS technique to densely apply in geoscience monitoring fields.

In this Letter we implement in-depth analyses for spatiotemporal strain profiles using DFOS with hybrid Brillouin-Rayleigh scattering in one water injection field test analogy to CGS process. We find that (1) strain magnitude and patterns are associated with injection scenario, and (2) potential injected water-transport footprint and affected regions coincide with those of analogy-based strain fronts. We show that downhole DFOS can provide new insights into imaging Earth's dynamics with unprecedented levels of detail, illuminating future farfield multi-well strain monitoring for large-scale long-term CGS projects.

2. Methodology

2.1. DFOS Principle with Hybrid Brillouin-Rayleigh Scattering

Downhole DFOS can monitor the entire surface-bottom profile that is impossible with point sensors or even wireline tools. Another is that glass fiber by its nature is immune to electromagnetic interference (Sun et al., 2018), can transmit data at high speeds, and can operate in extreme environments. All of these attributes make DFOS a robust solution for real-time long-distance in-situ life-of-well measurements.

Novel DFOS technology in this study is integrating Brillouin and Rayleigh backscattering into only one single-mode (SM) optical fiber (Figures 1 and S1A). It consists of synthetic Brillouin optical time domain reflectometry (S-BOTDR) and tunable wavelength

coherent optical time domain reflectometry (TW-COTDR), allowing SM fiber to simultaneously monitor strain and temperature along the fiber (Kishida et al., 2012). Here, S-BOTDR can achieve 10- cm spatial resolution (Nishiguchi et al., 2014) and TW-COTDR processing the same sensitivity as a conventional fiber Bragg grating sensor, is especially well-suited to detect small temperature and/or strain changes. (Wu et al., 2016). This hybrid system has their both advantages with higher spatial resolution of 5 cm than that of 1 m for other sensors.

S-BOTDR is based on single-ended spontaneous Brillouin scattering. Incident light will interact with acoustic phonons induced by thermal fluctuation or applied strain onto an optical fiber. Backscattered light has a Doppler shift (i.e., Brillouin frequency shift) in proportion to strain or temperature changes along the FO cable. Brillouin frequency shift, denoted as $\Delta\upsilon_B$, can be expressed as

$$\Delta\upsilon_B = \frac{\partial\upsilon_B}{\partial\varepsilon}\Delta\varepsilon + \frac{\partial\upsilon_B}{\partial T}\Delta T \quad (1)$$

where $\Delta\varepsilon$, ΔT, $\partial\upsilon_B/\partial\varepsilon$, $\partial\upsilon_B/\partial T$ are the strain and temperature increments, strain and temperature coefficients in Brillouin sensing, respectively.

TW-COTDR is based on single-ended time domain Rayleigh scattering. Power spectrum in TW-COTDR will occur due to refractive index fluctuations with random heterogeneity of glass density in the fiber core (Froggatt & Moore, 1998). Rayleigh frequency shift is obtained by comparing the measured value in reference state via cross-correlation (Kishida et al., 2012). The frequency shift $\Delta\upsilon_R$ induced by strain/temperature changes

can be depicted using the linear equation:

$$\Delta \upsilon_R = \frac{\partial \upsilon_R}{\partial \varepsilon} \Delta \varepsilon + \frac{\partial \upsilon_R}{\partial T} \Delta T \quad (2)$$

where $\Delta\varepsilon$, ΔT, $\partial \upsilon_R/\partial \varepsilon$, $\partial \upsilon_R/\partial T$ are the strain and temperature increments, strain and temperature coefficients in Rayleigh sensing, respectively.

Hybrid Brillouin-Rayleigh system can measure a separated temperature and strain using a single SM fiber by simultaneously solving Eqs. 1 and 2. For field monitoring for water injection via FO cables, a NeubreScope NBX-8000 optical interrogator (Neubrex Co., Kobe, Japan) was employed (Figure S1B). The sampling resolution and spatial resolution were set to 5 cm and 10 cm, respectively; the hybrid measurement accuracy was 10 με/0.5℃ over a long distance (~25 km) (Table S1). The strain and temperature coefficients for Rayleigh frequency shift from one-layer armored cable used in this field site were determined experimentally to -0.1535 GHz/με and -3.372 GHz/°C (Table S2).

2.2. Fiber Optic Cable Deployment and Water Injection Procedure

Three different types of FO cables were deployed behind casing of 300-m fibered well in Mobara, Chiba Perf., Japan (Figure 1A). Cable specifications and sensing modes are detailed in Sun et al., (2020) and Table S3. The FO cables ran from optical interrogator, which was set in a house near the testing site, in turn crossed bellows, underground horizontal polyvinyl chloride (PVC) pipes, bellows and external casing up to the 295-m-deep bottomhole (Figure 1B). These cables were single-end coupled well with external casing using specialized coupling protectors, fiber clamps and cable centralizers. Cables

were cemented within the annulus between casing and formation along the entire well depth; thereby full-bore monitoring strain variations can be realized. Note that all strains presented in this letter are vertical and relative strains recorded by one-layer armored cable (1A) via TW-COTDR sensing. Although Brillouin data were collected with S-BOTDR in these field tests, the main reason why they were not shown in this study is higher resolution and higher SNR of Rayleigh sensing than that of Brillouin sensing, which was concurrently logged to remove the strain and temperature cross-sensitivity effects with a single BrugSteel (Brugg Cables, Switzerland) FO cable (Sun et al., 2020).

Insert Figure 1 here.

Field water injection test was implemented between two adjacent vertical wells (5.5 m apart) with depths of 230 m and 300 m (Figure 1C). A 230-m-deep well acting as an injection well (IW #2) was drilled subsequent to 300-m-deep fibered monitoring well (MW #1). The whole geological section of MW #1 is described in Table S4. Water was injected through perforating fractures in IW #2 into targeted sand layers linking both wells, and gradually migrated to the fibered well, thus aiming to sense resulting strain responses via previously installed cables. Moreover, injection pressure and injection temperature were measured using pressure/temperature (P/T) sensors built into the drill pipe near the injection ports in IW #2 (Figure 1C).

Prior to water injection, borehole cementing and temperature equilibration were last for 25 days. Two injection tests were performed (Table S5). Additionally,

multi-instrument logging including electrical micro imager (EMI), radial cement bond log (RCBL), ultrasonic and radioactive logging were exploited conjointly with downhole DFOS monitoring in MW #1.

3. Results

3.1. In-Depth Analyses of Water Injection Scenario

During the whole injection process, injection rate was collected by wellhead flowmeter; injection pressure and injection temperature were acquired simultaneously employing P/T sensors installed in the borehole at 187.8 m depth in IW #2. Preinjected water was prepared in the storage tank with temperature of approximately 10 °C. Figure 2 shows detailed relationships between water injection scenarios with induced strain changes and provides new insights regarding how injection behavior affects interwell strain.

Based on the injection rate (Figure 2A), water injection test comprised six stages: pre-injection (**I**), low flowrate injection (**II**) with 12 L/min, unplanned stop (**III**), high flowrate injection (**IV**) with 120 L/min, moderate flowrate injection (**V**) with 80 L/min and post-injection (**VI**). At early stage (before 10:32), there was insignificant effect of injection pattern on the vertical strain, while for mid-late stage, injection water volume had a similar increasing pace with three strain profiles, indicating that cumulative mass was dominant effect.

Measurable frequency shifts resulted from changes in strain and temperature. Hence, in this study, water temperature was measured in IW borehole and via FIMT in MW #1.

Injection temperature varied from 16.5℃ to 12.9℃ with maximum difference of 3.6℃ (Figure 2B) as well as maximum temperature increment of 0.02℃ monitored by FIMT (Figure S4). Hence, although injection temperature changed relatively notable in IW, observed temperature increment in MW was so small that its effect could be negligible, mainly due to temperature equilibrium of migrating water between 5.5-m intervals.

Insert Figure 2 here.

Fluid pressure highly alters the reservoir-caprock geomechanics around the wellbore and largely reflects formation injectivity. Figure 2C shows details of injection pressure fluctuations and corresponding strain responses. Once injection was started, pressure variation constrained about 0.2 MPa and initial strain behave negative, implying that the formation experienced compressive deformation. With pressure increasing (i. e., **IV** stage), pressure increment rose to 0.5 MPa corresponding to +43 με strain @187.8 m along with maximum pressure gradient of 210 MPa/s, This situation was also applicable to post-injection with decreasing pressure. However, when injection pressure remained relatively stable, approximately 2.1 MPa accompanying ΔP=0.4 MPa and dP/dt=0 MPa/s (as marked with horizontal gray dashed line in Figure 2C), injection pressure had minimal influence on strain changes for this phase (**IV** and **V**). In addition, there were two notable leaps of pressure gradient occurred at 10:15 and 14:05, where strains just changed dramatically. This is the first time to quantify how injection scenario affected injection-induced strain. Thus, these findings further reveal that injection scenario plays a critical role in dominating water injection-driven strain magnitude and status

3.2. Finely Quantifying Spatiotemporal Strain Evolutions

S-BOTDR signal acted as reference for strain and temperature separation, TW-COTDR data sampled every 3 min via 1A cable with 10cm spatial resolution was converted into strain and displayed as a 2D contour (Figure 3). In-situ real-time high-resolution strain profile is useful to visualize in detail a 14-m-long water injection-impacted zone along a 300-m-deep borehole at the Mobara research site, Japan, using different combinations of instruments and cables. To deeper uncover latent information of optical data, strain responses should be finely dissected from spatial and temporal scales.

Time series of strain data from the post-processed TW-COTDR measurement at five depths during water injection test are shown in Figure 3A. Strain histories show strain variations had a similar pattern having high temporal repeatability. Generally, resulting strain would be larger in depth closer to the center of injection section. However, strain @188.6m was less than strain @185.9m, probably owing to formation heterogeneity. Thus, DFOS tool can concurrently track strain evolution at any point along a FO cable.

Optical data for all depths in MW #1 are shown in Figure 3B to image strain profile. In order to quantify spatiotemporal strain response, horizontal solid lines provide strain histories in five depths (Figure 3A) and vertical solid lines depict depth-based strain profiles in five time points (Figure 3C). As mentioned previously, although there were lower flowrate short injection (**II** in Figure 2), this stage can be classified into pre-injection with smaller strain. It is easy to find that large strains were mainly focused

on injection section and upper zone within 1 m distance. Due to the presence of fiber clamp and coupling protector (Sun et al., 2020), two strain anomalies occurred in 184.2 m and 189.2 m. Besides, based on EMI and resistivity logging in MW, visible strain weakening appeared at silt layers, thus demonstrating that impermeable silts could largely hinder water transport and strain propagation. These observations suggest that inexpensive DFOS has a great future potential to monitor fluid injection-induced geomechanical responses, e.g., wellbore integrity and caprock fracturing in depth.

Insert Figure 3 here.

Five depth-dependent strain profiles were selected to analyze nearfield strain evolution (Figure 3C). For injection zone (pink area), induced strain gradually enlarged with time; impacted zone was set within 182.2m~192.3 m (yellow area). Locations of two strain leaps agreed well with those shown in Figure 3B. Therefore, hybrid DFOS is useful to evaluate simultaneously near-wellbore strain evolutions.

Water was injected into a 2-m interval across perforation section, migrated along the 5.5m-long sand layer, flowed to the fibered well with different patterns resulted from heterogeneous 'arrival' pressures. Pressure fronts of injected water potentially pose different strain footprints logged by DFOS. In analogy with pressure front, strain front is defined in this study. Consequently, strain profile in Figure 2B was normalized based on linear rescaling method to map strain contour with [0, 1] interval (Figure 3D). Unified strain ($N\varepsilon_z^*(t)$) was calculated according to

$$N\varepsilon_z^*(t) = \frac{\varepsilon_z(t) - \varepsilon_z^{\min}}{\varepsilon_z^{\max} - \varepsilon_z^{\min}} \quad (3)$$

where $\varepsilon_z^{\max}$ and $\varepsilon_z^{\min}$ are the maximum and minimum FO strain values. Analogy-based strain fronts were plotted at normalized strains of 0.2 to 1.0 [-]. Note that strain front selection is arbitrary and little effect on the results. Clear-cut strain front allowed highlighting of a C-shaped pattern that has hitherto been not observed. First-arrival interface of each front was located in injection section (black dotted box in Figure3D). Notably, the strain fronts present two obvious fluctuations at 184.2 m and 189.2 m, which are reasonably consistent with previous results (Figures 3B and 3C). Moreover, convergence locations (horizontal white dotted lines in Figure 3D) also exactly matched the range of impacted zone in Figure 3C. It should be noted that there was a dip angle of ~10° between adjacent wells (see Figure 1C), which inevitably contributed to the downward extension of the impacted zone beyond the corresponding injection section.

4. Discussion and Concluding Remarks

In this study, an advanced hybrid Brillouin-Rayleigh distributed fiber-optic sensing tool was successfully deployed to in-situ monitor water injection test between two adjacent wells. Testing results showed that DFOS data provided a clear-cut spatiotemporal strain profile along the FO cables in a 300-m-deel well. Our observations demonstrated that injection volume and injection pressure significantly dominated strain magnitude and coverage. Potential injected water-transport footprint and strain impacted zone could be finely visualized via analogy-based strain fronts.

Most previous literature utilized DFOS method to monitor near-surface geoengineering (Shanafield et al., 2018). For example, vertical strain changes were sensed via DFOS in the shallow landslide (~15 m) (Kogure & Okuda, 2018) and groundwater pumping site (~145.3 m) (Zhang et al., 2018). By analogy with this water injection, supercritical CO_2 injection in deep reservoirs (over 800 m) will pose subsurface-surface strain changes. Therefore, this proven DFOS system can plot the complete strain map, which allows for establish quantitative links between surface deformations with subsurface injections at various future CGS-related geoenergy sites.

Lastly, our results subtly quantify cross-well strain data using this proposed hybrid DFOS system, detailed interpret strain evolutions related to injection scenario, mine implied information on fluid transport behaviors. These findings further highlight the wealth of additional detail in spatiotemporal strain dynamics recorded by DFOS and drive future far-field high-resolution crustal imaging applications in geophysics and hydrogeology.

Acknowledgments

This paper is based on results obtained from a project commissioned by the New Energy and Industrial Technology Development Organization (NEDO) and the Ministry of Economy, Trade and Industry (METI) of Japan. We would like to appreciate Takuma Ito (RITE) for providing laboratory grain size data for this project. The datasets used in this study are freely available online: https://figshare.com/s/040f576aacce5e059162.

References

Arts, R., & Vandeweijer, V. (2011). The challenges of monitoring CO2 storage. *The Leading Edge*, *30*(9), 1026–1033.

Arts, R., Eiken, O., Chadwick, A., Zweigel, P., van der Meer, L., & Zinszner, B. (2004). Monitoring of CO2 injected at Sleipner using time-lapse seismic data. *Energy*, *29*(9), 1383–1392.

Baatz, R., Bogena, H. R., Franssen Hendricks, H.-J., Huisman, J. A., Montzka, C., & Vereecken, H. (2015). Geomechanics of subsurface water withdrawal and injection. *Water Resources Research*, (51), 5974–5997.

Baldwin, C. S. (2014). Optical fiber sensing in the oil and gas industry: overcoming challenges. In *23rd International Conference on Optical Fiber Sensor* (Vol. 9157, pp. 9157C4-9157–4).

Bao, X., & Chen, L. (2012). Recent Progress in Distributed Fiber Optic Sensors. *Sensors*, *12*(7), 8601–8639.

Bense, V. F., Read, T., Bour, O., Le Borgne, T., Coleman, T., Krause, S., et al. (2016). Distributed Temperature Sensing as a downhole tool in hydrogeology. *Water Resources Research*, *52*(12), 9259–9273.

Chadwick, R. A., Arts, R., Eiken, O., Kirby, G. A., Lindeberg, E., & Zweigel, P. (2004). 4D Seismic Imaging of an Injected CO2 Plume at the Sleipner Field, Central North Sea. In *Petroleum Geology: North-West Europe and Global Perspectives—Proceedings of the 6th Petroleum Geology Conference* (Vol. 29, pp. 311–320).

Ferretti, A., Tamburini, A., Novali, F., Fumagalli, A., Falorni, G., & Rucci, A. (2011). Impact of high resolution radar imagery on reservoir monitoring. *Energy Procedia*, *4*, 3465–3471.

Froggatt, M. E., & Moore, J. (1998). High-spatial-resolution distributed strain measurement in optical fiber with rayleigh scatter. *Applied Optics*, *37*(10), 1735–40.

Jousset, P., Reinsch, T., Ryberg, T., Blanck, H., Clarke, A., Aghayev, R., et al. (2018). Dynamic strain determination using fibre-optic cables allows imaging of seismological and structural features. *Nature Communications*, *9*(1), 2509.

Karegar, M. A., Dixon, T. H., Malservisi, R., Yang, Q., Hossaini, S. A., & Hovorka, S. D. (2015). GPS-based monitoring of surface deformation associated with CO2 injection at an enhanced oil recovery site.

International Journal of Greenhouse Gas Control, *41*, 116–126.

Karrenbach, M., Kahn, D., Cole, S., Ridge, A., Boone, K., Rich, J., et al. (2017). Hydraulic-fracturing-induced strain and microseismic using in situ distributed fiber-optic sensing. In *Leading Edge* (Vol. 36, pp. 837–844). Society of Exploration Geophysicists.

Kersey, A. D. (2000). Optical fiber sensors for permanent downwell monitoring applications in the oil and gas industry. *IEICE Transactions on Electronics*, *83*(3), 400–404.

Kishida, K., Li, C. H., Nishiguchi, K., Yamauchi, Y., Guzik, A., & Tsuda, T. (2012). Hybrid Brillouin-Rayleigh distributed sensing system. In *SPIE* (Vol. 8421, pp. 84212G-8421–4).

Kogure, T., & Okuda, Y. (2018). Monitoring the Vertical Distribution of Rainfall-Induced Strain Changes in a Landslide Measured by Distributed Fiber Optic Sensing With Rayleigh Backscattering. *Geophysical Research Letters*, *45*(9), 4033–4040.

Kogure, T., Horiuchi, Y., Kiyama, T., Nishizawa, O., Xue, Z., & Matsuoka, T. (2015). Fiber optic strain measurements using distributed sensor system under static pressure conditions. *BUTSURI-TANSA(Geophysical Exploration)*, *68*(1), 23–38.

Lei, X., Xue, Z., & Hashimoto, T. (2019). Fiber Optic Sensing for Geomechanical Monitoring: (2)-Distributed Strain Measurements at a Pumping Test and Geomechanical Modeling of Deformation of Reservoir Rocks. *Applied Sciences*, *9*(3), 417.

Lellouch, A., Yuan, S., Spica, Z., Biondi, B., & Ellsworth, W. L. (2019). Seismic Velocity Estimation Using Passive Downhole Distributed Acoustic Sensing Records: Examples From the San Andreas Fault Observatory at Depth. *Journal of Geophysical Research: Solid Earth*, *124*(7), 6931–6948.

McColpin, G. R. (2009). Surface Deformation Monitoring As a Cost Effective MMV Method. *Energy Procedia*, *1*(1), 2079–2086.

Miah, K., & Potter, K. D. (2017). A Review of Hybrid Fiber-Optic Distributed Simultaneous Vibration and Temperature Sensing Technology and Its Geophysical Applications. *Sensors* , *17*(11), 1–25.

Murdoch, L. C., Germanovich, L. N., Dewolf, S. J., Moysey, S. M. J., Hanna, A. C., Kim, S., & Duncan, R. G. (2019). Feasibility of using in situ deformation to monitor CO2 storage. *International Journal of Greenhouse Gas Control*, *93*(December), 102853.

Nishiguchi, K., Li, C.-H., Guzik, A., & Kishida, K. (2014). Synthetic spectrum approach for Brillouin optical

time-domain reflectometry. *Sensors (Basel, Switzerland)*, *14*(3), 4731–4754.

Saito, H., Nobuoka, D., Azuma, H., Xue, Z., & Tanase, D. (2006). Time-lapse crosswell seismic tomography for monitoring injected CO2 in an onshore aquifer, Nagaoka, Japan. *Exploration Geophysics*, *37*(1), 30–36.

Schenato, L. (2017). *A Review of Distributed Fibre Optic Sensors for Geo-Hydrological Applications*. *Applied Sciences*.

Shanafield, M., Banks, E. W., Arkwright, J. W., & Hausner, M. B. (2018). Fiber-optic Sensing for Environmental Applications: Where We've Come From- and What's Possible? *Water Resources Research*.

Siriwardane, H. J., Gondle, R. K., & Bromhal, G. S. (2013). Coupled flow and deformation modeling of carbon dioxide migration in the presence of a caprock fracture during injection. *Energy and Fuels*, *27*(8), 4232–4243.

Sun, Y., Xue, Z., & Hashimoto, T. (2018). Fiber optic distributed sensing technology for real-time monitoring water jet tests: Implications for wellbore integrity diagnostics. *Journal of Natural Gas Science and Engineering*, *58*, 241–250.

Sun, Y., Xue, Z., Hashimoto, T., Lei, X., & Zhang, Y. (2020). Distributed Fiber Optic Sensing System for Well-Based Monitoring Water Injection Tests—A Geomechanical Responses Perspective. *Water Resources Research*, *56*(1), e2019WR024794.

Vasco, D. W., Rucci, A., Ferretti, A., Novali, F., Bissell, R. C., Ringrose, P. S., et al. (2010). Satellite-based measurements of surface deformation reveal fluid flow associated with the geological storage of carbon dioxide. *Geophysical Research Letters*, *37*(3), 1–5.

Verdon, J. P., Kendall, J.-M., Stork, A. L., Chadwick, R. A., White, D. J., & Bissell, R. C. (2013). Comparison of geomechanical deformation induced by megatonne-scale CO2 storage at Sleipner, Weyburn,

Verdon, J. P., Stork, A. L., Bissell, R. C., Bond, C. E., & Werner, M. J. (2015). Simulation of seismic events induced by CO2 injection at In Salah , Algeria. *Earth and Planetary Science Letters*, *426*, 118–129.

White, J. A., Chiaramonte, L., Ezzedine, S., Foxall, W., Hao, Y., Ramirez, A., & McNab, W. (2014). Geomechanical behavior of the reservoir and caprock system at the In Salah CO2 storage project. *Proceedings of the National Academy of Sciences*, *111*(24), 8747–8752.

Wu, Q., Nair, S., Shuck, M., Oort, E. van, Guzik, A., & Kishida, K. (2016). Advanced Distributed Fiber Optic Sensors for Monitoring Poor Zonal Isolation with Hydrocarbon Migration in Cemented Annuli. *Society of Petroleum Engineers*.

Xue, Z., Shi, J.-Q., Yamauchi, Y., & Durucan, S. (2018). Fiber Optic Sensing for Geomechanical Monitoring: (1)-Distributed Strain Measurements of Two Sandstones under Hydrostatic Confining and Pore Pressure Conditions. *Applied Sciences*, *8*(11), 2103.

Zhang, C.-C., Shi, B., Gu, K., Liu, S.-P., Wu, J.-H., Zhang, S., et al. (2018). Vertically Distributed Sensing of Deformation Using Fiber Optic Sensing. *Geophysical Research Letters*, *45*(21), 11,711-732,741.

Zhang, Y., & Xue, Z. (2019). Deformation-Based Monitoring of Water Migration in Rocks Using Distributed Fiber Optic Strain Sensing: A Laboratory Study. *Water Resources Research*, (55).

Zhang, Y., Xue, Z., Park, H., Shi, J. Q., Kiyama, T., Lei, X., et al. (2019). Tracking CO2 plumes in clay-rich rock by distributed fiber optic strain sensing (DFOSS): a laboratory demonstration. *Water Resources Research*, (55), 856–867.

Zoback, M. D., & Gorelick, S. M. (2012). Earthquake triggering and large-scale geologic storage of carbon dioxide. *Proceedings of the National Academy of Sciences* , *109*(26), 10164–10168.

394 # Figures

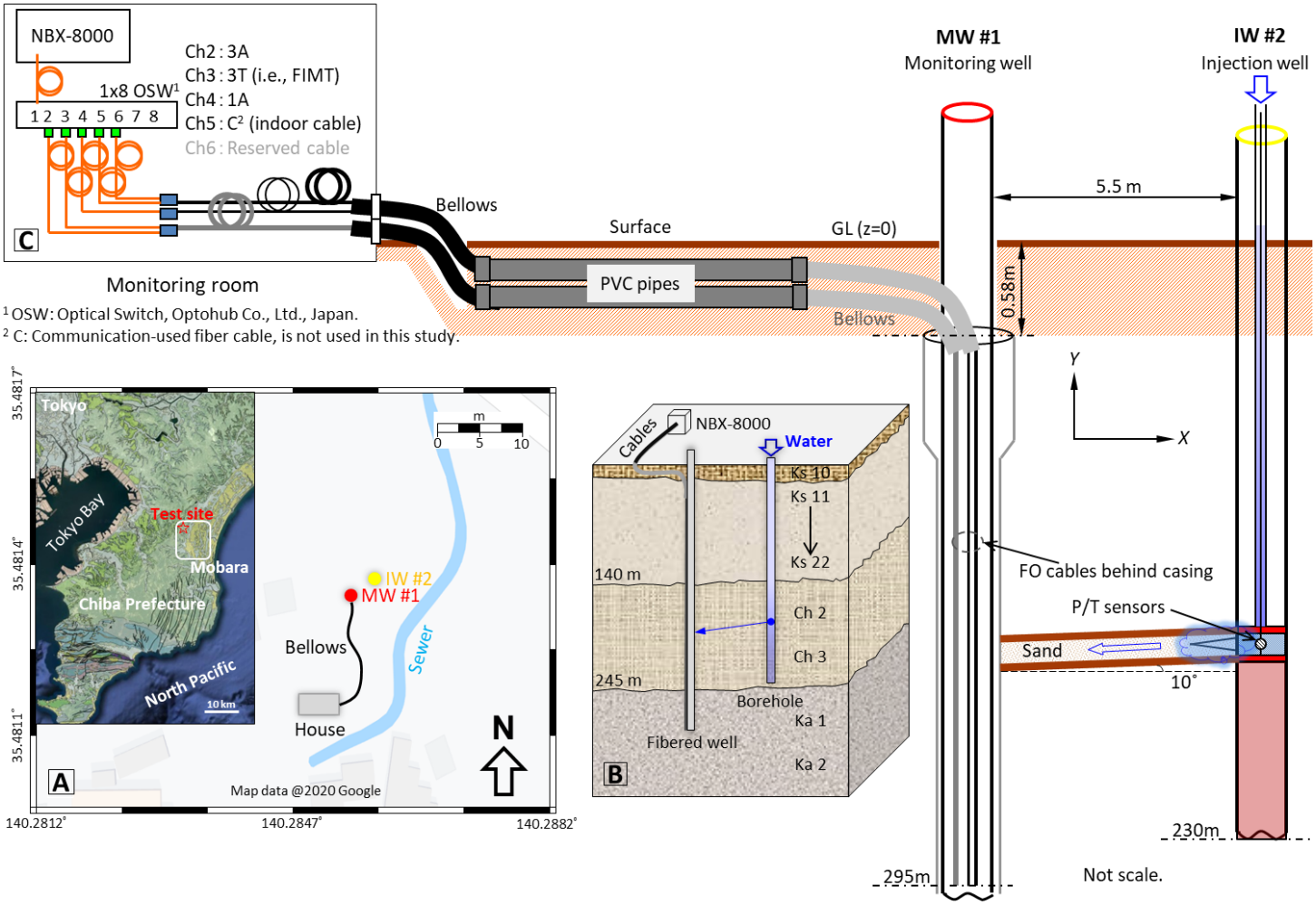

395 **Figure 1.** Field site and FO cables layout. (**A**) Map of water injection test. Inset depicts the location
396 of Mobara-shi, Chiba Prefecture, Central Japan (white box) and test site (red star). Red and yellow
397 circles denote monitoring well (MW #1) and injection well (IW #2). (**B**) 3D view of two adjacent
398 wells configuration and local stratigraphy. (**C**) Schematic illustration showing three whole-length
399 single-ended FO cables deployment and borehole geometry. Based on geophysical logging, dip
400 angle is about 10˚ for the injection formation. Note that 5.5 m is interwell distance at the surface.

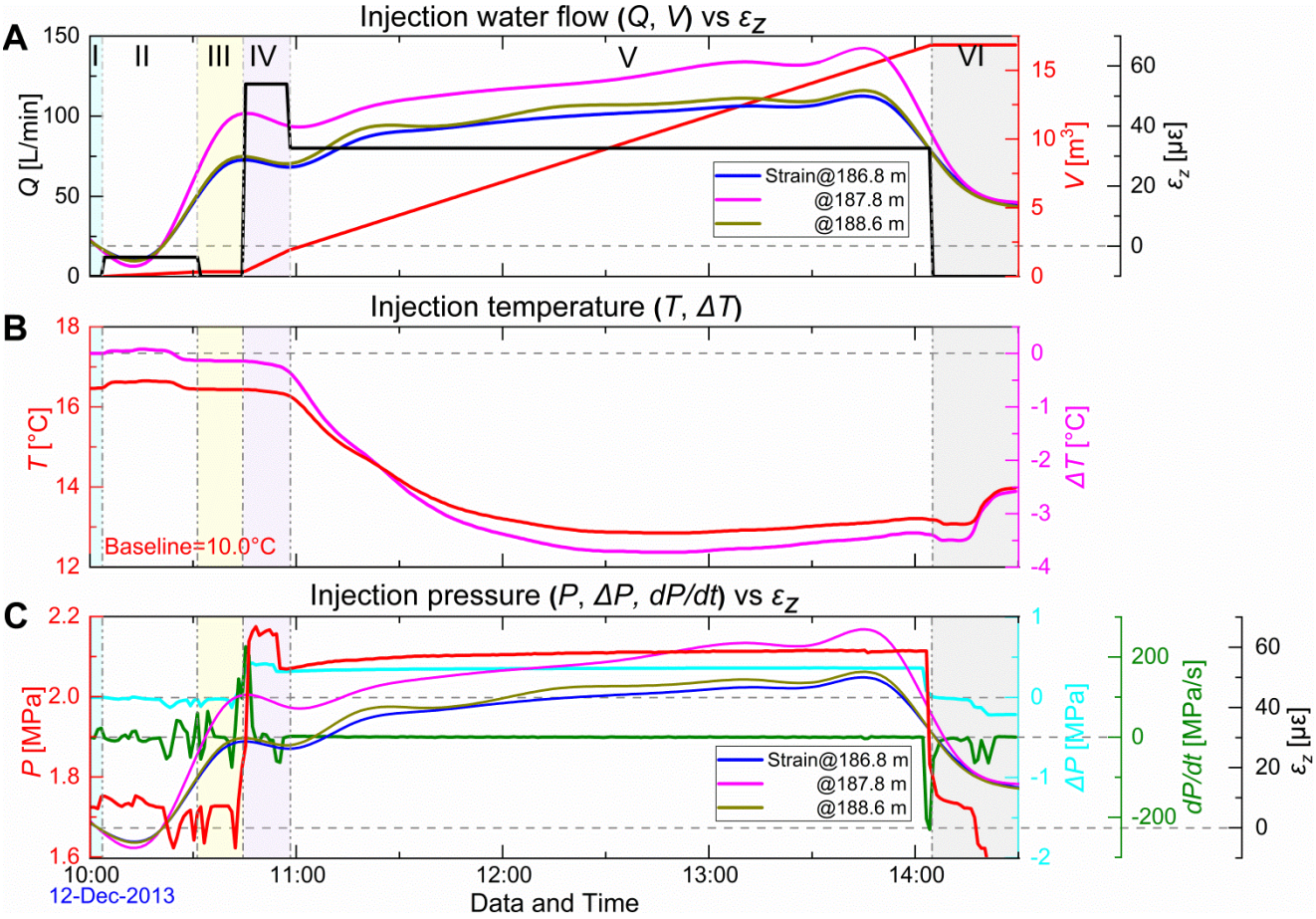

401 **Figure 2.** Multi-parameter observations of time-lapse water injection scenario with induced strains.

402 (**A**) Injection water flow reanalysis of IW #2-wellhead flowmeter data, injection rate *Q* (black) and

403 cumulative volume *V* =Q·t (red) show six injection stages (**I** to **VI**, marked with dashed vertical lines)

404 with strain profiles monitored at the depths of 186.8 m (blue), 187.8 m (magenta) and 188.6 m

405 (dark yellow), respectively in MW #1. (**B**) Temperature log of injected water recorded by built-in T

406 sensor near the injection ports in IW #2 (see Figure 1C) and corresponding temperature variation

407 (pink). Water temperature in the tank is about 10.0℃. (**C**) Injection pressure *P* (red), pressure

408 change *ΔP* (cyan) and pressure gradient *dP/dt* (olive) with three strain profiles, same as (A).

409 Pressure increment $\Delta P = P_t - P_0$.

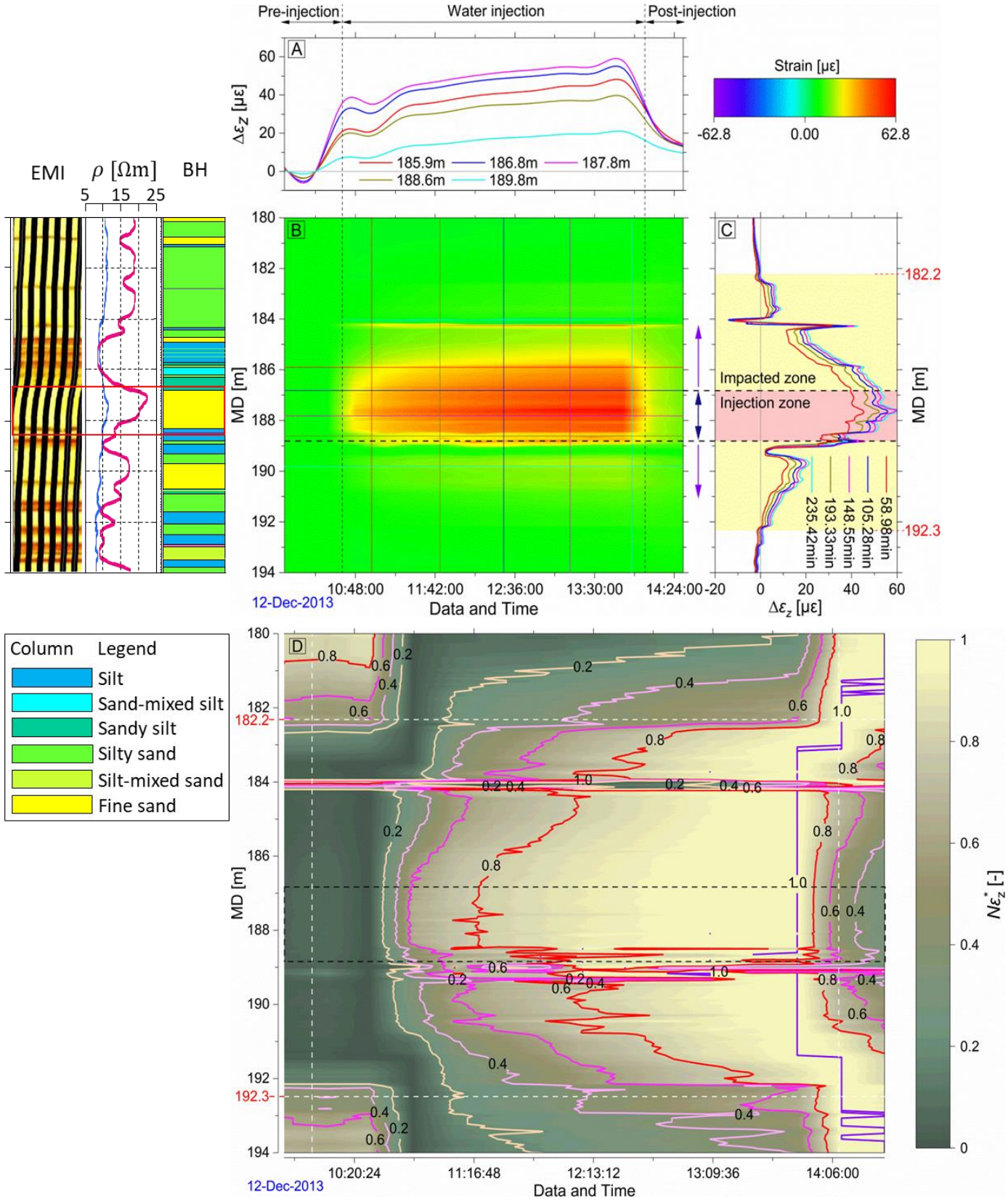

410 **Figure 3.** Spatiotemporal strain responses during the injection test and corresponding normalized

411 strain profile. (**A**) Time-varying strain histories at depths of 185.9 m (red), 186.8 m (blue), 187.8 m
412 (magenta), 188.6 m (dark yellow) and 189.8m (cyan), respectively. (**B**) Time-depth induced strain
413 image mapped with Rayleigh fiber-optic sensing recordings. Electrical micro imager (EMI) shows a
414 laminated sand/shale sequence of the formations in MW #1, generally brighter yellow colors for
415 more resistive sand-rich facies while darker brown colors for less resistive shale–rich facies. ρ:
416 electrical resistivity in formation. Borehole histogram (BH) is plotted based on EMI and resistivity
417 logs. Red solid box and black dotted lines denote injection section. (**C**) Depth-dependent strain
418 profiles at five injection time points of 58.98 min (red), 105.28 min (blue), 148.55 min (magenta),
419 193.33 min (dark yellow) and 235.42 min (cyan). Impacted zone is marked with yellow boxes. 182.8
420 m and 192.3 m are the critical depths of impacted zone. (**D**) Normalized strain profiles and
421 analogy-based strain fronts. Normalized strain contour lines of 0.2 (light yellow), 0.4 (light pink), 0.6
422 (pink), 0.8 (red) and 1.0 (violet) contour lines are plotted to exhibit potential strain fronts. Black
423 dotted box denotes injection section, and horizontal dotted lines are the convergence depths.

Figure 1.

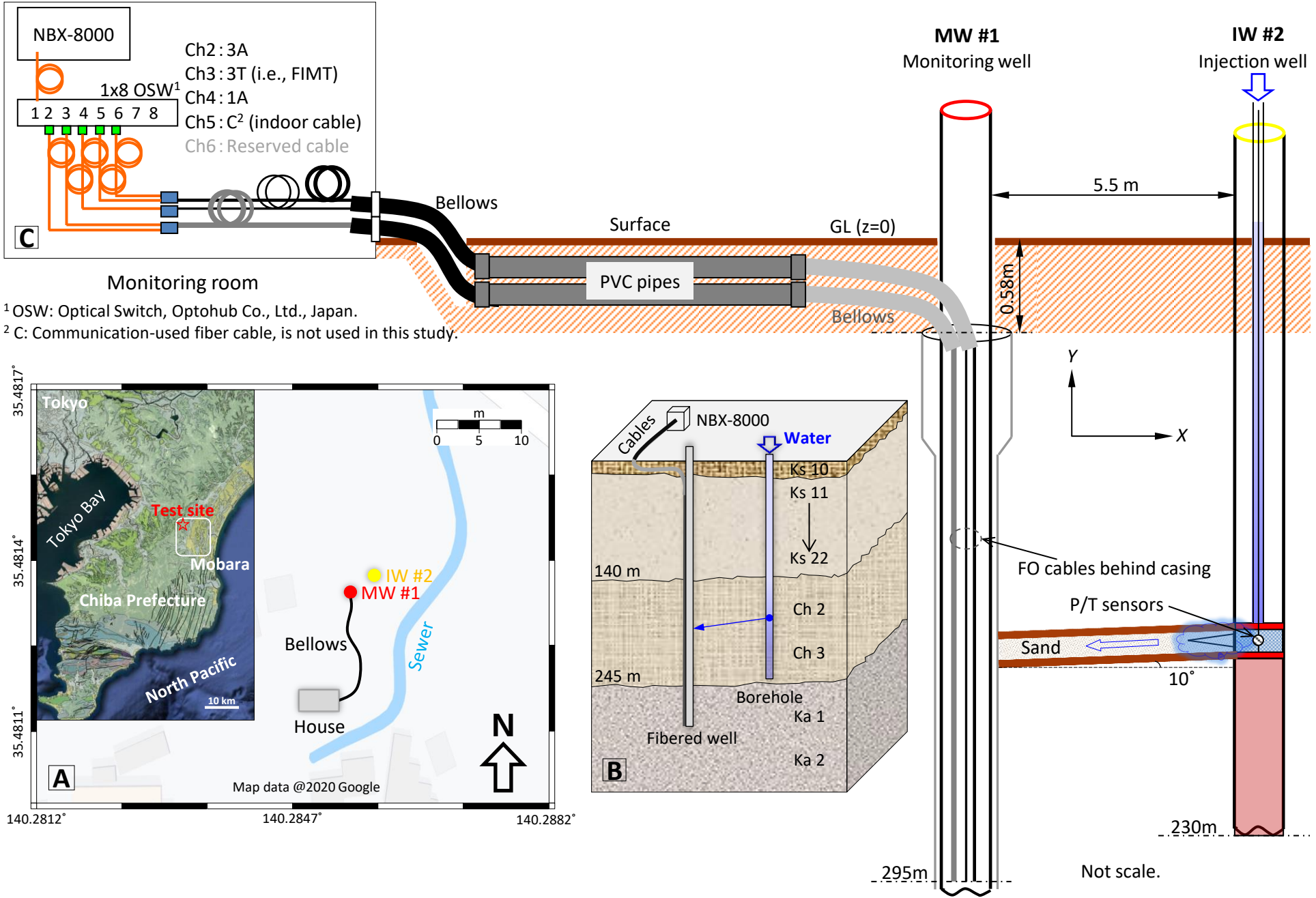

[1] OSW: Optical Switch, Optohub Co., Ltd., Japan.

[2] C: Communication-used fiber cable, is not used in this study.

Figure 2.

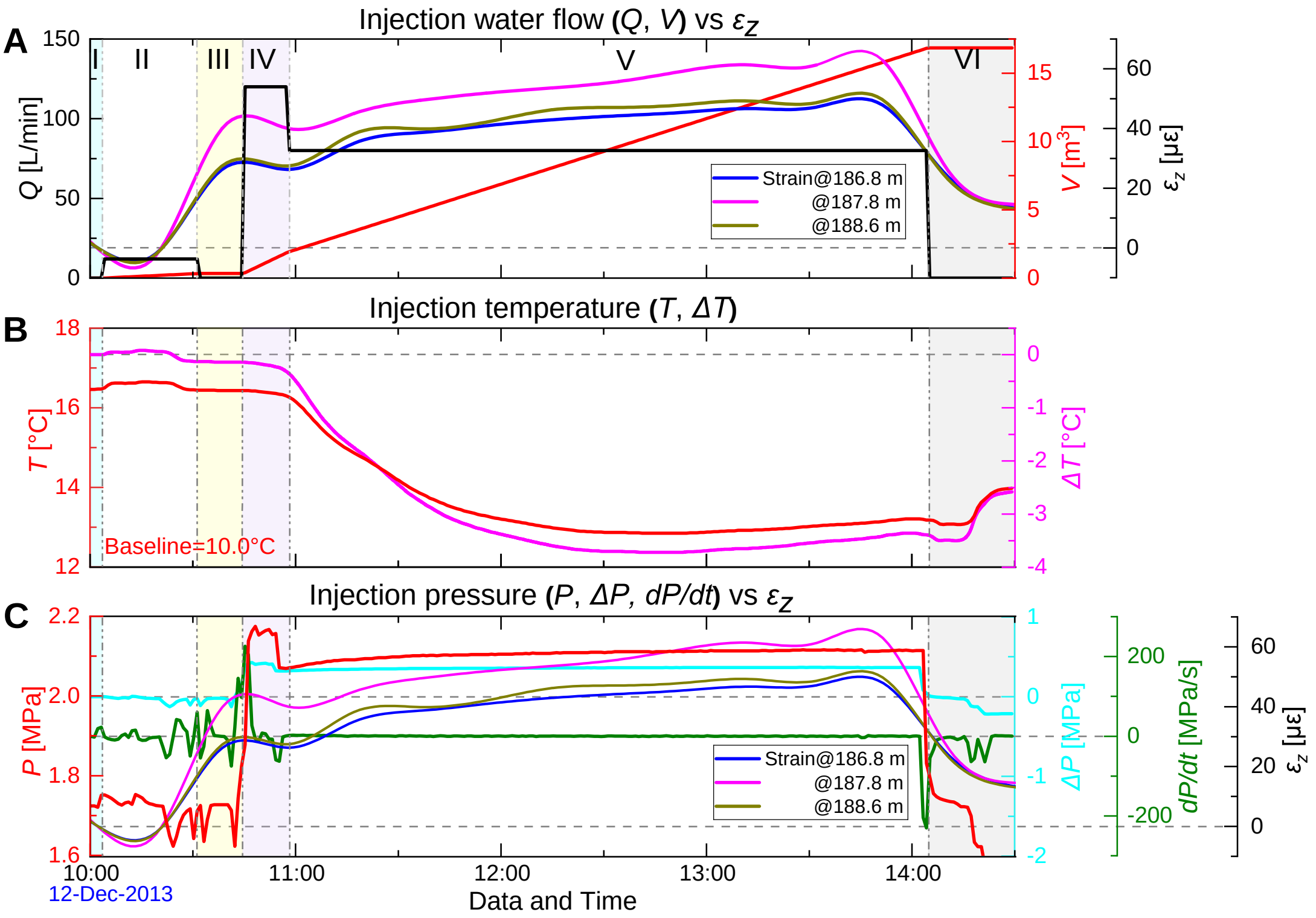
A
Injection water flow (Q, V) vs εZ
I
II
III
IV
V
VI
Q [L/min]
V [m3]
εz [με]
Strain@186.8 m
@187.8 m
@188.6 m
B
Injection temperature (T, ΔT)
T [°C]
ΔT [°C]
Baseline=10.0°C
C
Injection pressure (P, ΔP, dP/dt) vs εZ
P [MPa]
ΔP [MPa]
dP/dt [MPa/s]
εz [με]
Strain@186.8 m
@187.8 m
@188.6 m
10:00
11:00
12:00
13:00
14:00
12-Dec-2013
Data and Time

Figure 3.

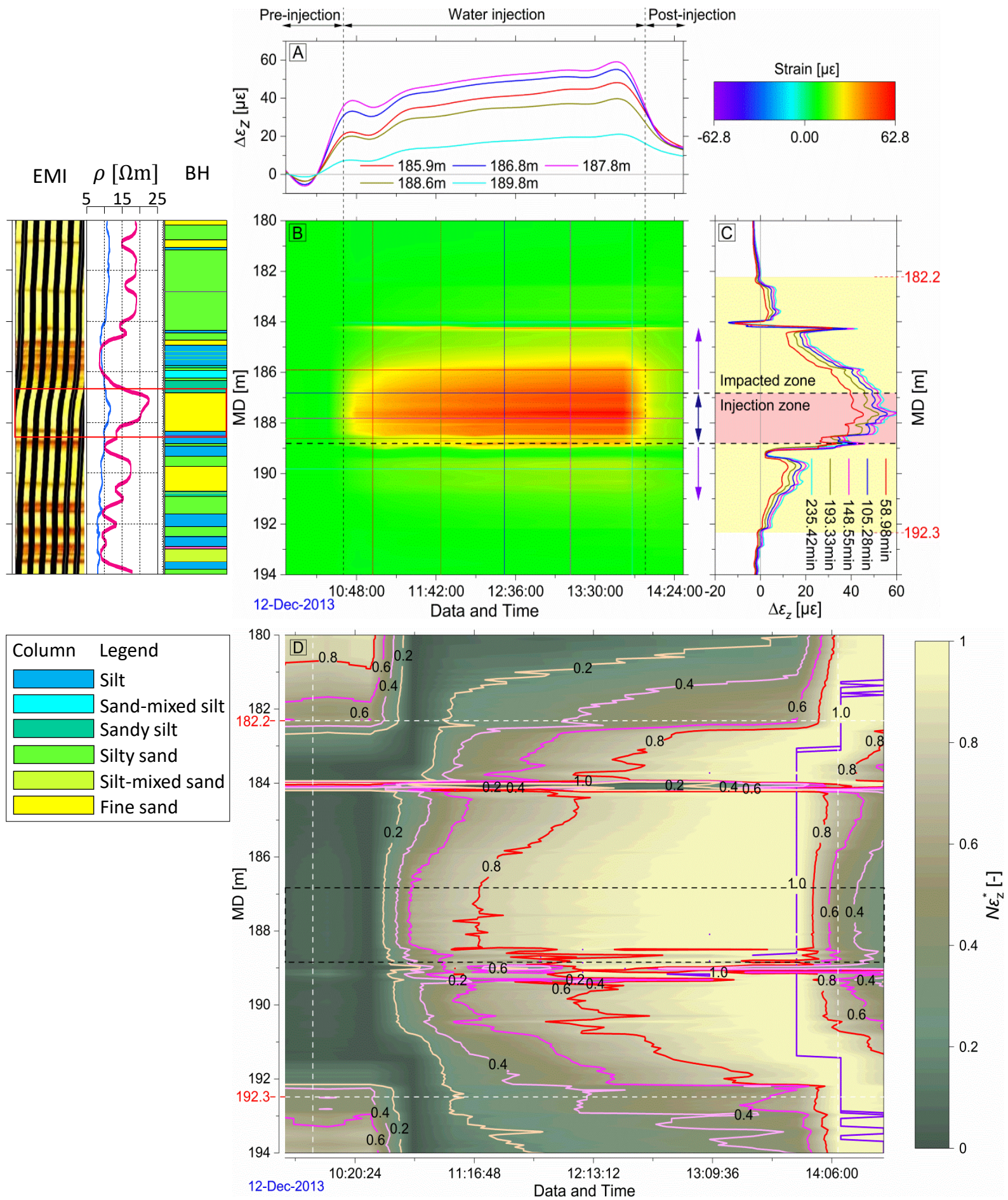
Pre-injection
Water injection
Post-injection
A
B
C
D
Strain [με]
-62.8
0.00
62.8
185.9m
186.8m
187.8m
188.6m
189.8m
EMI
ρ [Ωm]
BH
5
15
25
MD [m]
Impacted zone
Injection zone
182.2
192.3
58.98min
105.28min
148.55min
193.33min
235.42min
Δε_z [με]
12-Dec-2013
Data and Time
10:48:00
11:42:00
12:36:00
13:30:00
14:24:00
10:20:24
11:16:48
12:13:12
13:09:36
14:06:00
Column
Legend
Silt
Sand-mixed silt
Sandy silt
Silty sand
Silt-mixed sand
Fine sand
N_z* [-]